

Dispersion of inertial finite-size particles in turbulent open-channel flow

Petter Rikheim Benonisen 0, R. Jason Hearst 0 and Yi Hui Tee 0

¹Department of Energy and Process Engineering, Norwegian University of Science and Technology, Trondheim, Norway

Corresponding author: R. Jason Hearst, jason.hearst@ntnu.no

(Received 29 January 2025; revised 25 September 2025; accepted 13 October 2025)

Plastic pollution in our aquatic systems is a pressing issue, and the spread of these particles is determined by several factors. In this study, the advection and dispersion of negatively buoyant finite-size particles of four different shapes (spheres, circular cylinders, square cylinders and flat cuboids) and two sizes (6 and 9 mm) are investigated in turbulent open-channel flow. The volume, mass and characteristic length are fixed for each size. Four different turbulent conditions are considered, varying the free stream velocity U_{∞} = 0.25 and 0.38 m s⁻¹ and turbulence intensity $((u'/U)_{\infty} = 4\%$ and 9%). The particles are released individually from below the water surface. A catch-grid is placed along the bottom floor to mark the particle landing location. The average particle advection distance remains unchanged between the turbulence levels, suggesting that the mean settling velocity is independent of turbulence in this regime. Based on the root mean square of the landing locations, the particle dispersion varies with particle shape, size, settling velocity and turbulent flow conditions. For the square cylinders investigated in this work, the effect of particle shape on dispersion is difficult to predict at low flow velocities and turbulence intensities. As the turbulent fluctuations increase, the dispersion becomes more predictable for all shapes. An empirical expression is proposed to relate turbulent velocity fluctuations, integral length scales, particle settling velocity and particle size to streamwise dispersion. It is found that finite-size inertial particles do not disperse per simple turbulent diffusion, meaning that particle geometry has to be incorporated into dispersion models.

Key words: particle/fluid flow, turbulent flows

1. Introduction

Plastic pollution of many kinds, ranging from microplastics smaller than 5 mm to larger objects like plastic bags and bottles, has contaminated a wide range of Earth's ecosystems (Cressey 2016; Prata *et al.* 2020). A significant and increasing amount of plastic pollution ends up in the oceans. Individual plastic objects may retain their original shape or break down, adding to the plethora of particle geometries. While some of this waste floats near the surface, a considerable amount is negatively buoyant, either due to the inherent density of the plastic or the increased density from biofouling (Kaiser, Kowalski & Waniek 2017). Depending on the location, the concentration of debris floating on the ocean surface can reach up to 600 items km⁻², while on the ocean floor, this number can exceed 7700 items km⁻² (Galgani *et al.* 2015). Research into the transport and dispersion of plastic particles is an important part of understanding this global challenge (Sutherland *et al.* 2023). Under the waves, large-scale currents and free stream turbulence characterise ocean and river environments, affecting the spread of particulate matter along with particle size, shape, inertia and concentration, to name a few.

To model the transport of negatively buoyant particles by turbulent flow, the particle terminal vertical velocity (also known as the mean settling velocity, $|W_s|$) and dispersion need to be quantified. Past studies focused extensively on how the mean settling velocities of inertial particles are altered in homogenous isotropic turbulence (HIT). For spherical particles with a characteristic size, l, much smaller than the Kolmogorov scale, η , i.e. $l \ll \eta$, and particle-to-fluid density ratios much larger than unity $(\rho_p/\rho_f \gg 1)$, Maxey (1987) showed that $|W_s|$ increases under random flow fields compared with quiescent fluid. The ability for the mean settling velocity for these inertial particles to supersede that of the bulk flow is commonly explained as being due to preferential sweeping. This phenomenon, also known as fast-tracking, which results from the tendency of inertial particles to avoid vortex cores and oversample regions of downward-moving flow, has been observed in several numerical and experimental studies (Squires & Eaton 1991; Nielsen 1993; Petersen, Baker & Coletti 2019). In wall-bounded turbulence, the combined theoretical analysis and point-particle direct numerical simulation (DNS) by Bragg, Richter & Wang (2021) also showed that preferential sweeping enhances the average vertical velocity of inertial particles far from the wall. Near the wall, however, turbophoretic drift – arising from the combined effects of particle inertia and turbulence inhomogeneity - becomes the dominant mechanism.

The enhancement of settling velocity with turbulence is not present in all particleladen flows featuring HIT as confirmed by Ferran et al. (2023). The analytical study of small heavy particles by Dávila & Hunt (2001) showed that when $|W_s|$ is smaller than the root mean square (r.m.s.) of the fluid velocity fluctuations, u', i.e. $|W_s|/u' < 1$, the settling velocity increases in turbulent flows when compared with quiescent flow. Conversely, settling is hindered for particles with $|W_s|/u' > 1$, though to a lesser extent. For $|W_s|/u' > 4$, the change in $|W_s|$ is negligible. Good et al. (2014) reported similar results in their study combining experimental data with DNS of water droplets in air turbulence. The reduction in $|W_s|$ when $0 \lesssim |W_s|/u' \lesssim 0.1$ was due to nonlinear drag effects. Fornari et al. (2016) studied slightly negatively buoyant finite-size $(l > \eta)$ spherical particles with $0.19 \le |W_s|/u' \le 4.81$ in HIT numerically. The settling velocity was altered by changing ρ_p/ρ_f . They found significant reductions in $|W_s|$ compared with quiescent flow at low $|W_s|/u'$. As $|W_s|/u'$ increased, the reduction became less prominent. The reductions in settling velocity in all turbulent cases were due to the vertical drag induced by the particle cross-flow velocity. Lighter particles experience the highest cross-flow velocities and thus more drag than heavier particles that fall along more vertical paths.

Particle–turbulence interactions are multiscale in nature and depend on particle parameters and turbulent scales beyond $|W_s|$ and u' alone (Balachandar & Eaton 2010; Tom & Bragg 2019). These results highlight the importance of considering a wider range of parameters when investigating settling behaviour.

The field of settling anisotropic particles in turbulent flow is largely unexplored, in contrast to flow regimes concerning spherical particles. Most existing research explores simple ellipsoids (Voth & Soldati 2017), disks (Esteban, Shrimpton & Ganapathisubramani 2020) and fibres (Giurgiu et al. 2024), to name a few. A recent study by Tinklenberg, Guala & Coletti (2024) on thin millimetre-sized disks falling in HIT in air with $\rho_p/\rho_f \approx 10^3$ reported that $|W_s|$ was reduced by up to 35 % in strong turbulence compared with quiescent flow, with the largest disks being most influenced. This reduction is contrary to the case of disks settling in HIT in water, where $\rho_D/\rho_f = 2.7$ (Esteban et al. 2020). In this case, settling was enhanced, highlighting the importance of the density ratio on settling behaviour. Slight variations in geometry can also have severe effects on settling. Chan et al. (2021) found that thin curved particles resembling bottle fragments exhibited reduced settling velocities in conditions similar to Esteban et al. (2020). Meanwhile, Shaik & van Hout (2023) investigated inertial and length effects of rigid fibres of different lengths in turbulent channel flow. They found that as the fibre length and Stokes number $(St = \tau_p/\tau_f)$, where τ_p is the particle response time to the surrounding fluid and τ_f is a flow time scale, usually the Kolmogorov time scale in HIT or viscous time scale in channel flow) increased, the particles tended to lag in the flow away from the wall. For finite-size particles of various shapes, a recent volumetric study by Tee, Dawson & Hearst (2025) shows that the downwash from a group of freely falling particles increases the settling velocity of the trailing particles, regardless of their shape.

Particle dispersion – like the settling velocity – is a function of particle size, inertia, geometry and flow conditions. Tracers, defined as neutrally buoyant particles with $l \ll \eta$ or $St \ll 1$, act like fluid elements, and their dispersion is directly related to turbulent velocity fluctuations. Gustavsson, Einarsson & Mhelig (2014) theoretically demonstrated that even when particle inertia is negligible $(St \to 0)$, geometry remains important to particle dynamics in turbulent flows. They showed that persistent regions of high vorticity in turbulence lead to significantly higher tumbling rates for disks than for rods (see also Jeffery (1922)). In HIT, particle dispersion was found to be larger for heavy particles than for fluid elements in inertia-dominated (high St) flow regimes (Wang & Stock 1993). When $|W_s|/u'$ dominated over St, however, the particle dispersion was reduced compared with fluid elements. Large-eddy simulations of sub-Kolmogorov size neutrally buoyant spherical particles, disks and needle-like particles (fibres) in turbulent channel flow were performed to investigate the effects of shape on particle dynamics (Njobuenwu & Fairweather 2015). They found that the dispersion of fibres more closely resembled tracers. Disks with a low aspect ratio, 0.1 < AR < 1.0, on the other hand, were more dispersed by turbulence than spherical particles. In the previously discussed studies of Esteban et al. (2020) and Chan et al. (2021) concerning disks and curved particles, respectively, dispersion also increased when turbulence was added. Shin & Koch (2005) performed DNS on neutrally buoyant fibres in turbulent flow. Similarly to Njobuenwu & Fairweather (2015), they found that the fibres dispersed identically to tracers for particles with $l < \eta$, however, as l increased beyond η , particles became less sensitive to small-scale rapidly fluctuating motions, and their translational diffusivity was diminished.

For wall-bounded flows where small inertial particles remain in suspension for most of the time, e.g. sediment transport in rivers, the streamwise dispersion coefficient increases with $|W_s|$ (Sumer 1974). In these flows, particles are prevented from permanently depositing on the wall by a balance between $|W_s|$ and turbulent resuspension (Baker &

Coletti 2022). This happens when $|W_s| < \kappa u_{\tau}$, where u_{τ} is the friction velocity, and κ is the von Kármán constant, which may be the case for high-drag inertial particles. The increase in dispersion for faster settling particles may seem counterintuitive, as a higherinertia particle might be expected to have a greater resistance to turbulent fluctuations. The increased dispersion is due to the higher likelihood of heavier particles spending more time in the near-wall region, where turbulent fluctuations are greater. In contrast, a lighter particle is likely to spend more time in the free stream where the velocity gradient and turbulent fluctuations are small (Sumer 1974). Tee, Barros & Longmire (2020) investigated finite-size spheres (1.006 $\leq \rho_p/\rho_f \leq$ 1.152) released from rest along a glass wall in a turbulent boundary layer experimentally. For both lifting and wallinteracting particles, spanwise forces in the boundary layer were found to be important as particles were significantly dispersed in this direction. In addition, suspended spheres were observed to occasionally descend faster than their mean settling velocities in quiescent flow. Meanwhile, studies by van Hout (2013) and van Hout et al. (2022) also observed particles interacting with coherent structures typically found in turbulent boundary layers, like hairpin packets and transverse and longitudinal vortices. These interactions, which induced fluctuations in particle velocity, further support the notion that boundary layer effects are important to dispersion.

The recent experimental study by Clark et al. (2023) investigated the dispersion of negatively buoyant anisotropic particles (rods, unit-aspect-ratio cylinders and disks) in currents with and without gravity waves. There were two main particle parameters under investigation in this study, the first being the aspect ratio, which has been found to significantly influence the falling styles of disks (Auguste, Magnaudet & Fabre 2013). The second was the Archimedes number, i.e. the ratio of gravitational to viscous forces, $Ar = (\rho_p/\rho_f - 1)l^3g/v^2$, where g is gravitational acceleration and v is the fluid kinematic viscosity. The particle characteristic sizes were in the range 3 mm $\leq l \leq$ 7 mm. They found that the presence of surface gravity waves enhanced particle dispersion for all particle types, except in the case of the largest cylinders. The observed effect was significant, with the thinnest rods increasing their dispersion by a factor of four. In a later parametric study (Sunberg et al. 2024), they found that for ellipsoid particles, the settling-wave time scale ratio, i.e. the Stokes drift velocity to settling velocity ratio, led to the greatest range in dispersion values. The conclusions drawn from these two papers are that particle shape and volume, as well as wave parameters, must be taken into account when particle dispersion is modelled.

While most research is directed towards settling particles in HIT or inertial particles within the turbulent boundary layer (Brandt & Coletti 2022), the settling and dispersion of particles due to free stream turbulence above the boundary layer have not been studied extensively. The effects of sizes and shapes on top of particle inertia can also affect particle dynamics. In an attempt to fill the gap, we conduct an experimental study to investigate the advection and dispersion of inertial anisotropic finite-size particles ($l > \eta$) in a turbulent open channel. An active grid is used to generate free stream turbulence with different turbulent intensities and integral length scales. Negatively buoyant particles of various sizes and shapes are released individually into the turbulent flow. All particles are of high St and belong to the settling dominated regime $|W_s|/u' > 1$. The goal is to study the competing effects between the flow and particle parameters on particle settling and dispersion. Section 2 describes the experimental set-up and measurement techniques used in the study. Sections 3 characterises the various turbulent flow conditions considered. Section 4 discusses the effects of turbulent conditions as well as particle shape and size on settling behaviour, while § 5 tackles particle dispersion. In the final part of § 5,

an empirical model obtained by dimensional nonlinear regression for the particle dispersion is presented and discussed qualitatively.

2. Methodology

2.1. Experimental set-up

The experiments were conducted in the water channel in the Fluid Mechanics Laboratory at the Norwegian University of Science and Technology (NTNU). The test section of this channel is 11.2 m long in the x-direction, 1.8 m wide in the y-direction with a height of 1 m in the z-direction. For this experiment, the water depth was set to $h_w = 0.53$ m. The channel is of a recirculating design with a free surface and a 4:1 contraction upstream of the test section. Past this contraction, at the start of the test section, an active grid is used to produce tailored turbulent conditions (see Jooss et al. (2021) for more details on the facility). The active grid allows for the generation of higher $Re_L = U_{\infty}L/\nu$ and $Re_{\lambda} = u'_{\infty} \lambda/\nu$ than achievable with other approaches, e.g. passive grids; U_{∞} is the free stream velocity, u'_{∞} is the standard deviation of the free stream velocity fluctuations, L and λ are the integral length scale and Taylor microscale, respectively. The resulting turbulence characteristics are primarily dependent on the grid Reynolds number $Re_M = U_{\infty} M/\nu$ and Rossby number, $Ro = U_{\infty}/\Omega M$, where M is the grid mesh size and Ω is the mean frequency of the grid-rod rotation (Larssen & Devenport 2011; Hearst & Lavoie 2015). Increasing Ro results in higher turbulence intensities $(u'/U)_{\infty}$. The active grid used in this study is the same as the one used by Jooss et al. (2021), which is based on the design of Makita (1991). The grid is biplanar with 18 vertical rods and four horizontal rods immersed in the water in this experiment. These rods can be rotated individually by stepper motors. The mesh size is M = 100 mm. Attached to the rods are diagonally oriented square wings with two holes – one on each side of the rod – which prevent full blockage and reduce the load on the motors. Tailored turbulent conditions are created by controlling the rotational frequency at which the grid rods spin. A grid setting is defined by a central frequency, Ω , and a bandwidth, ω . Each vertical rod of the active grid rotates at a random frequency in the range $\Omega \pm \omega$ with a top-hat distribution. For all cases in the present study, $\omega = \Omega/2$. At random intervals, a rod changes its frequency to rotate at a new speed in either the same or opposite direction. The horizontal rods remain static in the open position with wings parallel to the flow. Generally, lower values of Ω produce higher turbulence levels except in the limit of $\Omega \to 0$ (Larssen & Devenport 2011; Hearst & Lavoie 2015). A wedge spanning the width of the channel and extending 2 m downstream of the active grid is placed at the water surface to dampen any surface waves directly produced by the grid. A schematic of the test section of the water channel is provided in figure. 1.

Negatively buoyant particles are dropped one by one from an automated release mechanism 30 mm below the water surface at h = 0.50 m. The mechanism is positioned at x/M = 50. This location was chosen for being sufficiently far downstream to avoid neargrid effects from the active grid (Comte-Bellot & Corrsin 1966; Jooss *et al.* 2021). The homogeneity of the free stream in the produced flows is explicitly demonstrated in § 3. The particle release mechanism consists of a 65 mm wide triangular box with perforated walls. Particles are released individually from rest by the actuation of a mechanical gate in intervals of 20 s. Initial particle orientations are randomised while their starting locations remain constant. From their release point, particles descend to the channel floor and settle in a particle catch-grid. The catch-grid is 3.55 m long in the streamwise direction, 0.60 m wide in the spanwise direction, and 7 mm high in the vertical direction, with rectangular cells where $\Delta x = 22$ mm and $\Delta y = 11$ mm are the streamwise and spanwise cell side

P.R. Benonisen, R.J. Hearst and Y.H. Tee

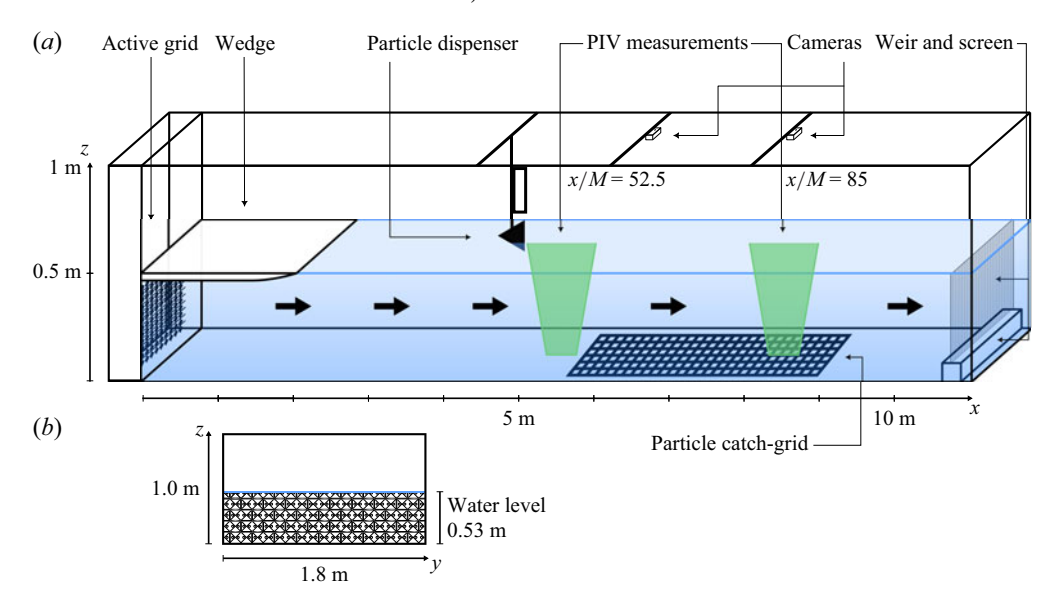


Figure 1. Schematic of the water channel test section. Note that the vertical height has been exaggerated in (a) for readability. Panel (b) accurately represents the active grid dimensions.

lengths, respectively. The catch-grid is centred in the spanwise direction and located such that its upstream end is 0.375 m downstream of the release point. The catch-grid is wide enough that less than 1% of particles settled outside its bounds. Two Logitech C925e web cameras were mounted on top of the water channel along the streamwise distance to record the particle landing locations. The centre of the grid cell in which a particle lands defines its settling location (x_p, y_p) . This measurement technique is based on the study by Clark *et al.* (2023) who investigated the effects of gravity waves on particle dispersion. When quantifying the dispersion, we focus on the first landing location of the particle after hitting the wall. Hence, the catch-grid also helps to prevent the particles from moving along the wall due to near-wall interactions (see also Baker & Coletti (2021) and Tee & Longmire (2024)). A weir and a fine mesh screen are installed at the very end of the test section to catch any stray particles and produce a hydraulic jump to prevent surface wave reflections.

2.2. Particle parameters

The particles investigated in this study come in four shapes similar to those in Tee et al. (2025): spheres, circular cylinders, square cylinders and flat cuboids, with two characteristic sizes of $l_1 \approx 6$ and 9 mm. They are 3D-printed with a Formlabs Form 3 resin printer using Formlabs' Tough 1500 Resin with a density of $\rho_p = 1150 \,\mathrm{kg} \,\mathrm{m}^{-3}$ ($\rho_p/\rho_f = 1.15$). The 3D-printer's resolution is 50 μ m. For each characteristic size, the different particles were designed to have the same volume and characteristic length, l_1 . This was done to better investigate the effect of shape on results separately from size effects. As a consequence, Ar has the same form for all particles as l_1 is equal to the diameter of a volume-equivalent sphere. Particle lengths were measured using callipers with an accuracy of $\pm 0.025 \,\mathrm{mm}$, and the average length based on 20 particles of each type was computed. The aspect ratio, AR, is taken as the ratio between the side length of the axis of rotational symmetry and its perpendicular side length. The value of AR is above unity for prolate shapes (circular and square cylinders), below unity for oblate shapes (flat cuboids) and equal to unity for perfect spheres. Due to print imperfections, the spherical particles

	1				$\bigcup_{I_2} I_1$		$\bigcup_{l_1} b_2$	
Property	Sphere		Circular cylinder		Square cylinder		Flat cuboid	
Symbol	0	•	Δ	A	\Diamond	•		
l_1 (mm)	6.05(7)	9.15(5)	6.35(4)	9.46(6)	6.36(5)	9.46(6)	6.33(5)	9.42(5)
l_2 (mm)	_	_	4.82(4)	7.19(3)	4.31(3)	6.41(3)	3.12(5)	4.65(3)
AR	1.02(1)	1.031(7)	1.32(1)	1.32(1)	1.48(2)	1.48(1)	0.493(9)	0.494(4)
m (g)	0.131(2)	0.437(2)	0.135(1)	0.451(2)	0.134(1)	0.456(2)	0.134(2)	0.457(2)
$ W_s \text{ (m s}^{-1})$	0.156(8)	0.20(1)	0.12(1)	0.14(2)	0.10(1)	0.12(1)	0.088(6)	0.104(8)
Re_p	890	1720	720	1250	600	1070	520	920
C_D	0.49	0.43	0.79	0.88	1.27	1.35	1.12	1.23
C_D^*	0.49	0.43	0.77	0.85	1.09	1.17	1.42	1.57

Table 1. Particle parameters. Parentheses denote error estimates in the least significant digit computed as the standard deviation of the measurements. For the variables l_1 , l_2 and m, measurement errors have been included using Pythagorean sums. Symbols listed in the table are used to denote particle shape and size in the subsequent figures.

used in this study have aspect ratios slightly above unity. Aspect ratio was not explicitly varied for a given shape in the present investigation. The particle mass was obtained by measuring and averaging 20 particles of each type using a high-precision piezoelectric scale with a measurement error of ± 0.0005 g. The particle geometric parameters are provided in table 1.

Trajectories of settling particles in quiescent flow were measured separately using a stereoscopic imaging and calibration technique as explained by Muller et al. (2020). Two GoPro Hero 12 Black cameras were set up looking from the sidewall to triangulate the three-dimensional positions of the settling particles. The videos were captured at 50 frames per second with 5.3K resolution (5312 × 2988 pixels). For each particle type, 15-20 trajectories were captured (not shown here). For a single particle trajectory, the terminal settling velocity, $|W_s|$, is taken as the descent's mean vertical velocity after reaching a quasisteady state. Here, smoothing was applied to the trajectories prior to differentiation using a third-order Savitsky-Golay filter with a 15-point stencil (Buchner et al. 2021). Differences in velocities calculated with and without smoothing are an order of magnitude lower than the measurement standard deviations (see also Schneiders & Sciacchitano (2017)). This settling velocity is used to obtain the particle Reynolds number, $Re_p = |W_s| l_1/\nu$, and mean settling drag coefficient, $C_D = mg(1 - \rho_f/\rho_p)/\nu$ $(1/2\rho_f|W_s|^2A)$, where A is the flow-facing projected area as described in Goral et al. (2023). In essence, A is the broadest projected area of a particle, e.g. the large square face of the flat cuboids or the curved side of the circular cylinder. The drag coefficient employing the projected area of a volume-equivalent sphere, $C_D^* = mg(1 - \rho_f/\rho_p)/$ $(1/2\rho_f|W_s|^2A^*)$, where $A^* = \pi(l_1/2)^2$ is also included for reference. The values of C_D for both spherical particles agree with the $Re-C_D$ relation of Clift, Grace & Weber (1992). Values of $|W_s|$, Re_p , C_D and C_D^* are also listed in table 1 with the other particle parameters.

The particle Stokes number, $St = \tau_p/\tau_f$, are estimated based on $\tau_p = \rho_p l_1^2/18\nu\rho_f$ (Brandt & Coletti 2022) and $\tau_f = \tau_{\eta,\infty} = \sqrt{\nu/\epsilon_\infty}$ where $\tau_{\eta,\infty}$ is the Kolmogorov time scale in the free stream. The free stream dissipation rate of the turbulent kinetic energy (ϵ_∞) was estimated using second-order structure functions. In all flow cases, the

Kolmogorov length scale is in the range $0.4 \,\mathrm{mm} \lesssim \eta \lesssim 0.7 \,\mathrm{mm}$, which is close to the lower limit of the characteristic range for small-scale, wind-driven oceanic turbulence (Jiménez 1997). The particle image velocimetry (PIV) data used to obtain $\tau_f = \tau_{\eta,\infty}$ is described and expanded upon in § 2.3. For all cases, the particle Stokes numbers are above unity, i.e. St > 1. The value of St increases with turbulence and particle size. For spheres, they fall within the range $4 \lesssim St \lesssim 14$ for 6 mm particles and $9 \lesssim St \lesssim 31$ for 9 mm particles.

2.3. Flow measurements

The settling and dispersion of particles are investigated at two different free stream velocities, $U_{\infty} \approx 0.25 \, \mathrm{m \ s^{-1}}$ and $0.38 \, \mathrm{m \ s^{-1}}$ and active grid settings $\Omega = 0.05 \pm 0.025 \, \mathrm{Hz}$ and 1.0 ± 0.5 Hz. To characterise the flow, PIV was employed at two locations: between the particle dispenser and the catch-grid at x/M = 52.5, and near the downstream end of the catch-grid at x/M = 85.0 (see figure 1). The measurements were performed to obtain streamwise and wall-normal velocity fields (u and w, respectively). To capture the entire vertical span of the flow field, two LaVision Imager MX 25-megapixel cameras were placed on top of each other, viewing the flow through the sidewall. Both cameras were fitted with a Sigma 105 mm focal length lens. A Litron Nano L 200-15 PIV Nd:YAG laser produced a 200 mm wide laser sheet. The flow was seeded with 40 µm Dynoseeds polystyrene particles. LaVision DaVis 10 was used for the acquisition and processing of PIV data. The two-dimensional vector field was obtained using standard cross-correlation with initial and final window sizes of 96×96 pixels and 64×64 pixels, respectively. With 50% overlap, the PIV vector spacing was 2.1 mm. The uncertainty associated with PIV correlation calculations was less than $\sim 3 \ \mathrm{mm \ s^{-1}}$ for the streamwise velocity component based on the uncertainty approach of Wieneke (2015). Among the four flow cases, the PIV acquisition frequencies were varied between 0.5 and 0.9 Hz such that the subsequent image pairs were independent and uncorrelated. In total, 2000 image pairs were taken per case. From these vector fields, free stream parameters were calculated. This included the free stream velocity U_{∞} and the r.m.s. of the streamwise and wall-normal velocity fluctuations, u'_{∞} and w'_{∞} , respectively. These quantities were used to obtain the free stream turbulence intensity, $(u'/U)_{\infty}$, anisotropy estimate, $(u'/w')_{\infty}$, and Reynolds number based on the hydraulic diameter, $Re_D = U_{\infty} D_h / v$, where D_h is the cross-sectional area of the channel divided by the wetted perimeter. These free stream parameters are taken as quantities averaged over the vertical region 330 mm $\leq z \leq$ 420 mm. Additionally, the bulk velocity U_b and the boundary layer shape factor $H = \delta^*/\theta$ are calculated from the velocity profile, where δ^* and θ are the displacement and momentum thicknesses, respectively. These values are reported in table 2 and discussed further in § 3.

In tandem with the PIV measurements used to obtain mean quantities, laser Doppler velocimetry (LDV) measurements were taken 0.2 m upstream of each PIV measurement location, i.e. at x/M = 50.5 and x/M = 83.0, at z = 410 mm. A 60 mm FiberFlow probe from Dantec Dynamics was used in backscatter mode with a beam expander and a lens with a focal length of 500 mm. Two lasers measured the streamwise and vertical velocities, u and w, respectively. The laser measuring u has a wavelength of 514.5 nm, while the laser measuring w has a wavelength of 488 nm. As the LDV and PIV measurements were obtained simultaneously, they both relied on the same seeding particles. Average LDV acquisition rates are dependent on the seeding density and were within the approximate range of 45-55 Hz between cases. The sampling duration was set to 40 min. From these long, higher frequency acquisitions, the large scales, L_{11} , were taken as the integral of the autocorrelation function of the velocity fluctuations up to the first zero-crossing. The intermediate scales defined by the Taylor microscale, λ , were calculated from

x/M	U_{∞} (m s ⁻¹)	U_b (m s ⁻¹)	$(u'/U)_{\infty}$ (%)	$(u'/w')_{\infty}$	$Re_D \times 10^{-5})$	L ₁₁ (mm)	Re_{λ}	Н	
52.5	0.244	0.229	4.38	1.5	3.08	67.0	220	1.22	•
52.5	0.246	0.232	8.50	1.7	3.11	210.4	468	1.18	
52.5	0.374	0.352	4.00	1.4	4.70	64.5	230	1.21	
52.5	0.375	0.355	9.11	1.8	4.73	292.0	664	1.18	
85.0	0.250	0.224	3.83	1.6	3.15	48.2	178	1.75	
85.0	0.251	0.226	6.71	1.4	3.17	178.1	319	1.71	
85.0	0.381	0.341	3.19	1.4	4.79	54.4	140	1.77	
85.0	0.382	0.344	7.18	1.5	4.81	265.2	391	1.69	

Table 2. Flow parameters at upstream and downstream locations for all four flow conditions. The right-hand column relates flow conditions to the colour legend used in all figures.

$$\lambda^2 = 15\nu \left(\frac{u_{\infty}^{\prime 2}}{\epsilon_{\infty}}\right). \tag{2.1}$$

The Taylor microscale is used together with u'_{∞} to define the turbulent Reynolds number Re_{λ} .

3. Flow characterisation

Figure 2 shows the mean streamwise velocity and turbulence intensity profiles. In figures 2(a) and 2(c), four different flow cases measured at the upstream location x/M = 52.5 are compared. The mean velocity profiles for the four cases at two different bulk velocities and with different turbulence intensities shown in figure 2(a) are roughly collapsed, suggesting Reynolds number effects are not significant. Likewise, the fluctuating velocity profiles in figure 2(c) show good agreement when comparing the different bulk velocities. Not shown here are velocity and turbulence intensity profiles at x/M = 85.0, which collapse similarly. In figures 2(b) and 2(d), we focus on the flow case at $U_{\infty} \approx 0.38 \,\mathrm{m \ s^{-1}}$ with $(u'/U)_{\infty} \approx 9 \,\%$ as an example and compare the profiles at x/M = 52.5 with and without the release mechanism, as well as at the downstream location x/M = 85.0. For the upstream velocity profiles, a noticeable mean velocity deficit (see figure 2b) and increased turbulence fluctuations (see figure 2d) below the release height $z/h_w = 1$ arise from the wake of the release mechanism, which protrudes 30 mm below the surface. With the mechanism removed, the free stream is recovered below $z/h_w \approx 0.8$. Between the upstream and downstream locations, the particle catch-grid on the bottom wall acts as a roughness element, damping the near-wall mean velocity profile (figure 2b) while enhancing velocity fluctuations (figure 2d). Otherwise, across all three measurements, a significant portion of the flow, nominally 50 %-75 %, is 'free stream' wherein the mean velocity and the turbulence intensity (see figure 2b,d) do not change substantially in the z-direction.

Single-pixel PIV calculations (Westerweel, Geelhoed & Lindken 2004) were applied to the near-wall field at the upstream measurement location, the results of which are shown in figure 2(a). Applying the method of Rodríguez-López et al. (2015) and Esteban et al. (2017) to the single-pixel data yielded estimates of the friction velocity $u_{\tau} = (\tau_w/\rho_f)^{0.5}$, where τ_w is the wall shear stress. The obtained values of the friction velocity were approximately $u_{\tau} = 0.01$ and 0.015 m s⁻¹ at $U_{\infty} \approx 0.25$ and 0.38 m s⁻¹, respectively. This yielded $Re_{\tau} = u_{\tau}\delta/\nu$ in the range $2600 \lesssim Re_{\tau} \lesssim 4500$, where δ is the boundary layer thickness. The values of U_{∞} and U_b are slightly higher in the high-turbulence cases as

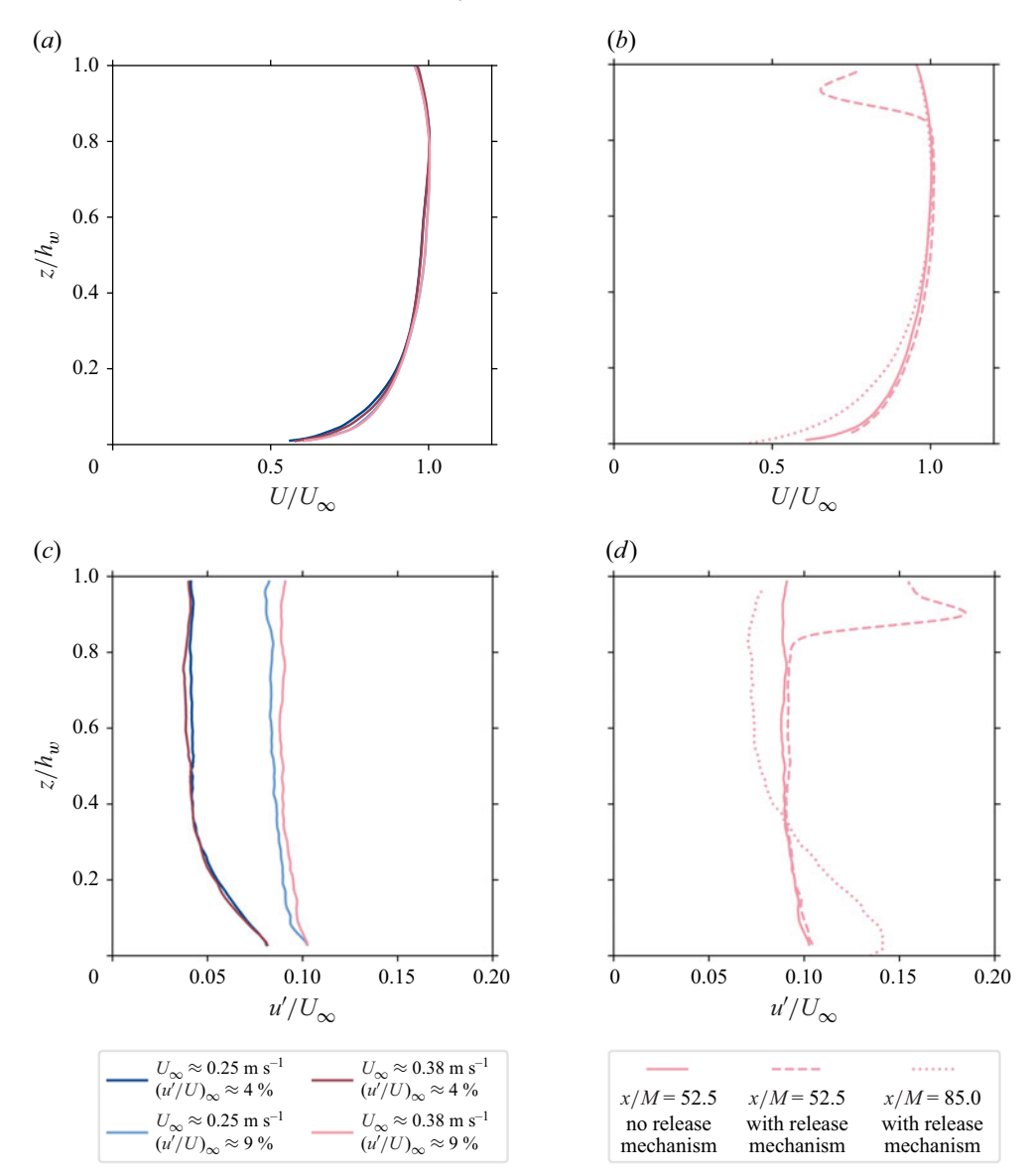


Figure 2. Wall-normal profiles of the (a,b) normalised mean streamwise velocity component $U(z)/U_{\infty}$ and (c,d) turbulence intensity $u'(z)/U_{\infty}$. Panels (a) and (c) show profiles at x/M=52.5 for all flow cases while panels (b) and (d) show the differences between upstream profiles at x/M=52.5 – with and without the release mechanism installed – and downstream profiles at x/M=85.0 for a sample case $(U_{\infty}\approx 0.38 \, \mathrm{m \ s^{-1}}, \, (u'/U)_{\infty}\approx 9 \, \%)$. Points in the near-wall region in (a) are results from single-pixel PIV.

compared with the low-turbulence cases. The increase in U_b is small, less than 2% for both $U_\infty \approx 0.25~\mathrm{m~s^{-1}}$ and $0.38~\mathrm{m~s^{-1}}$. The effects of this on the particle mean settling locations will be discussed in § 4. Free stream anisotropy is in the range $1.4 \leqslant (u'/w')_\infty \leqslant 1.8$. The increase in the shape factor between the upstream and downstream locations is large compared with the boundary layer study of Jooss *et al.* (2021), which was performed in the same facility, because the catch-grid of the present investigation represents a roughwall where H increases with surface friction (Castro 2007) in contrast to the smooth wall

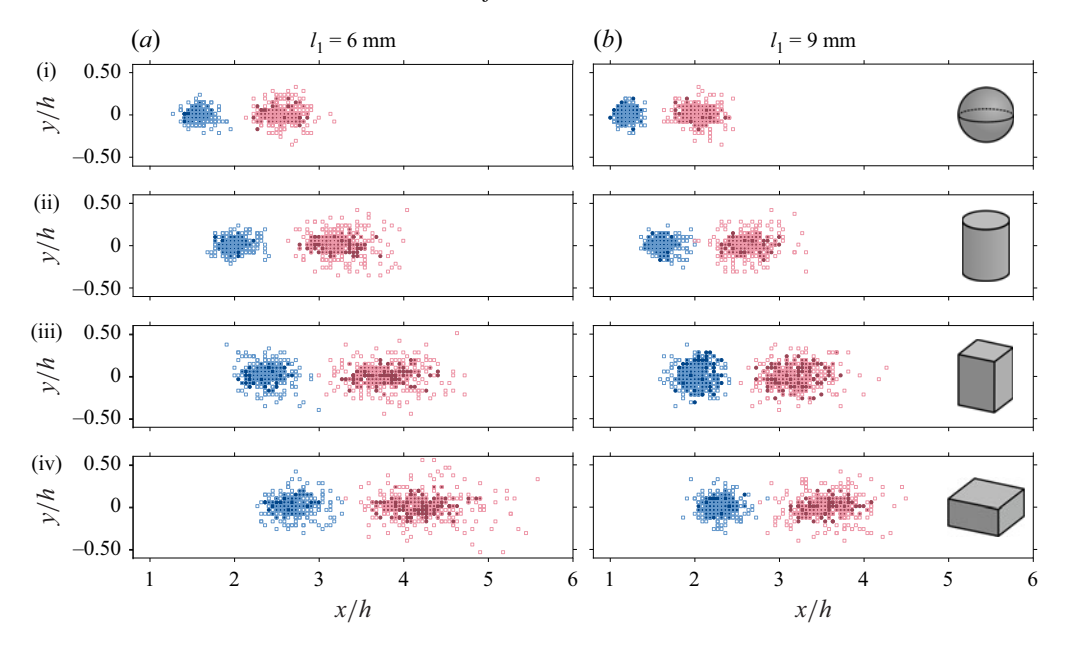


Figure 3. Scatter plots of all 32 experimental cases. Panels (a) and (b) depict scatter for 6 mm and 9 mm particles, respectively. Blue markers denote $U_{\infty} = 0.25 \,\mathrm{m\,s^{-1}}$, while red markers correspond to $U_{\infty} = 0.38 \,\mathrm{m\,s^{-1}}$. The dark circles and light squares are scatter of particles in low turbulence ($(u'/U)_{\infty} \approx 4 \,\%$) and high turbulence ($(u'/U)_{\infty} \approx 9 \,\%$), respectively. Subpanels (i) to (iv) correspond to spheres, circular cylinders, square cylinders and flat cuboids, respectively. Axes are equal in aspect ratio.

of Jooss *et al.* (2021). This change in shape factor is therefore to be expected. Note that integral length scales increase with turbulence intensity. This will be discussed further in § 5. An overview of the flow characteristics from PIV and LDV measurements is presented in table 2. In the subsequent discussion, the different turbulent cases are referred to by their turbulence intensity for convenience.

4. Mean settling location and vertical velocity

The particle settling locations for all experimental cases are presented in figure 3. In each experimental case, 200 particles were dropped. Clark *et al.* (2023) reported good convergence in wavy flows with only 100 particle drops per case. Subsampling half of each case of the present experimental data also revealed good convergence with particle dispersion values lying within 0 %–12 % of the final value. To avoid extreme events heavily influencing the results of the particle drops, data points lying more than 3.5 standard deviations away from the mean have been removed. The number of such outliers is low, less than 1 % in all cases. From the scatter plots of figure 3, one can immediately get a general idea of the effect of changing particle size and shape, advection velocity and turbulence intensity.

It is clear that particle shape is important. The anisotropic particles tend to travel farther than the spheres, with flat cuboids being advected farther than square cylinders, followed by circular cylinders. This is expected due to the differences in drag experienced by the particles (see table 1). Larger particles tend to travel a shorter distance than smaller particles before being deposited on the channel floor. Drag forces increase with surface area. However, this drag is superseded by the increased gravitational forces due to the higher mass, ensuring the net downward force increases, and particles are advected a

P.R. Benonisen, R.J. Hearst and Y.H. Tee

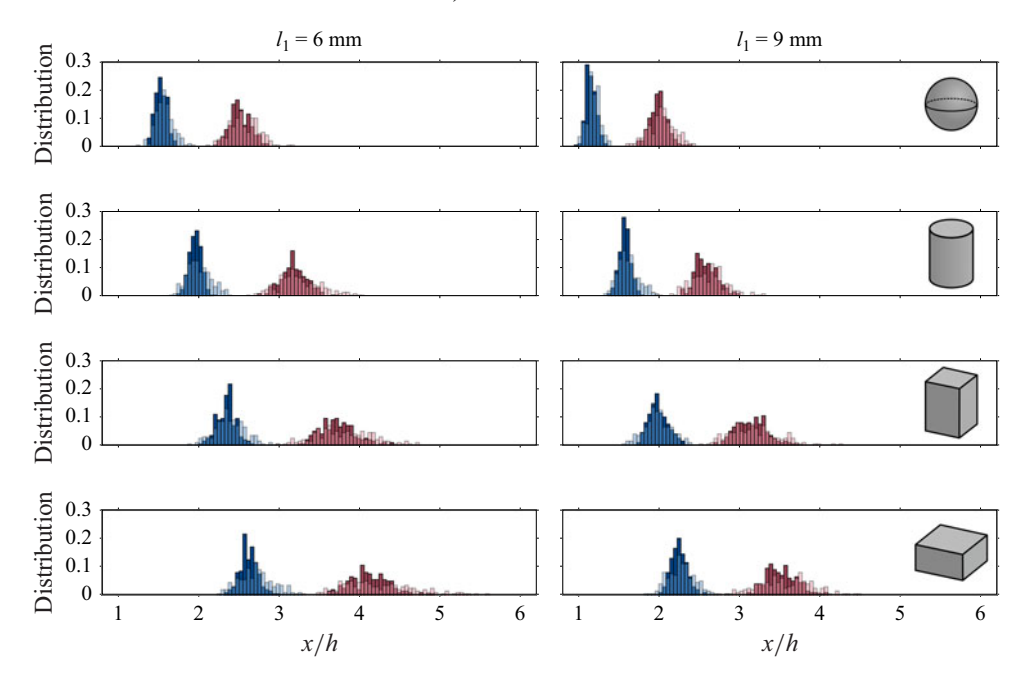


Figure 4. Discrete probability distributions of the streamwise settling locations of particles, x_p . Bins represent the physical locations and widths of the particle catch-grid cells, while the y-axes show the relative frequency. Dark blue (\bullet) and light blue (\bullet) bars correspond to low and high turbulence intensity at $U_\infty \approx 0.25 \,\mathrm{m \ s^{-1}}$, respectively, while dark red (\bullet) and pink (\bullet) bars correspond to low and high turbulence at $U_\infty \approx 0.38 \,\mathrm{m \ s^{-1}}$.

shorter distance. Unsurprisingly, increasing the free stream velocity also increases the value of the mean streamwise settling location, \overline{x}_p . As U_∞ increases by approximately 50% from \sim 0.25 to 0.38 m s⁻¹, \overline{x}_p increases by 55%–70% depending on shape. This velocity change enhances the advection of spherical particles the most, followed by circular cylinders, square cylinders, and flat cuboids. In other words, those particles that travel the shortest distance before being deposited are also the ones whose advection is most enhanced by changes in U_∞ . In all experimental cases, the mean spanwise settling location, \overline{y}_p , lies close to the channel centreline. The histograms of figure 4 show the discrete probability distributions of particle settling locations, $n_{cell}/n_{tot.}$, where n_{cell} is the number of particles landing in cells with a given streamwise settling location and $n_{tot.}$ is the total number of particles dropped per case.

When it comes to the effect of turbulence on the settling of particles, figures 3 and 4 indicate that it is significant. Mainly, the dispersion, (σ_x, σ_y) taken as the r.m.s. of the streamwise and spanwise particle settling locations, respectively, is greatly affected by increasing turbulence intensity. For example, the flatter distributions of the high turbulence cases in figure 4 imply larger streamwise dispersion. This relationship will be discussed in detail in § 5. What is not immediately apparent from looking at the particle scatter is how turbulence influences \overline{x}_p . A measure of how the mean settling location changes with respect to turbulence for a given particle and U_{∞} is the ratio $\overline{x}_{p,h}/\overline{x}_{p,l}$, where the subscripts '1' and 'h' correspond to low turbulence intensity (4%) and high turbulence intensity (9%), respectively. Accounting for the marginal changes in U_b between the high and low turbulence intensity cases measured at the same U_{∞} , the mean settling ratio becomes

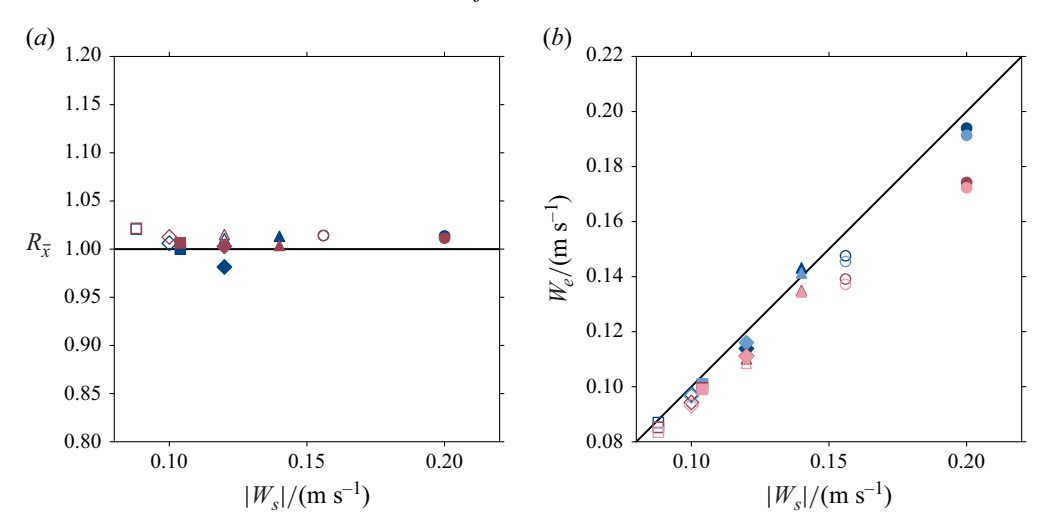


Figure 5. (a) Mean settling ratio $R_{\overline{x}}$ for all particles at $U_{\infty} = 0.25 \,\mathrm{m \, s^{-1}}$ () and $U_{\infty} = 0.38 \,\mathrm{m \, s^{-1}}$ (). (b) Estimated mean vertical particle velocity W_e (4.2) plotted against the quiescent settling velocity $|W_s|$. Dark blue () and light blue () markers correspond to low and high turbulence intensity at $U_{\infty} \approx 0.25 \,\mathrm{m \, s^{-1}}$, respectively, while dark red () and pink () markers correspond to low and high turbulence at $U_{\infty} \approx 0.38 \,\mathrm{m \, s^{-1}}$. Circle , spheres; triangle , circular cylinders; diamond , square cylinders; square , flat cuboids. Solid markers, 9 mm particles; hollow markers, 6 mm particles.

$$R_{\overline{x}} = \frac{\overline{x}_{p,h}}{\overline{x}_{p,1}} \frac{U_{b,1}}{U_{b,h}}.$$

$$(4.1)$$

The results of this comparison between high- and low-turbulence cases are plotted in figure 5(a). This investigation shows that the mean values remain relatively unchanged even though an individual particle's settling location may be greatly affected by changing turbulent conditions, reflected in the increased scatter visible in figure 3. With this in mind, it is prudent to ask whether \overline{x}_p can be predicted using parameters determined in laminar or quiescent flow. For example, if one knew the value of U_b and $|W_s|$ a priori, could one estimate, with some certainty, how far a particle will be advected on average before being deposited? In a simplified scenario, assuming constant horizontal and vertical velocity, the time required for a particle to travel the horizontal distance \overline{x}_p at a velocity of U_b equals \overline{x}_p/U_b . This length of time must equal the one required to travel the vertical distance h at some estimated vertical velocity, W_e , i.e. h/W_e . The expression for W_e then becomes

$$W_e = \frac{h}{\overline{x}_p} U_b. \tag{4.2}$$

The values of W_e are plotted against $|W_s|$ in figure 5(b). The diagonal line indicates $W_e = |W_s|$. The lower values of W_e than $|W_s|$ for particles advecting in the faster flow (red markers) as compared with the slower flow (blue markers) show that there appears to be some dependencies on U_b . This is likely due to the bulk velocity not capturing the full effect of the differences in the velocity profiles as the particles descend. Moreover, between turbulence levels (darker and lighter markers), W_e remains relatively unchanged. Turbulent effects on the mean particle settling velocity are, in other words, negligible compared with other parameters like U_b and particle geometry in this particular particle—turbulence flow regime. This result stands in contrast to the theory of Maxey (1987) and Bragg *et al.* (2021) on small inertial particles, however, it agrees with Fornari *et al.* (2016), who found that the

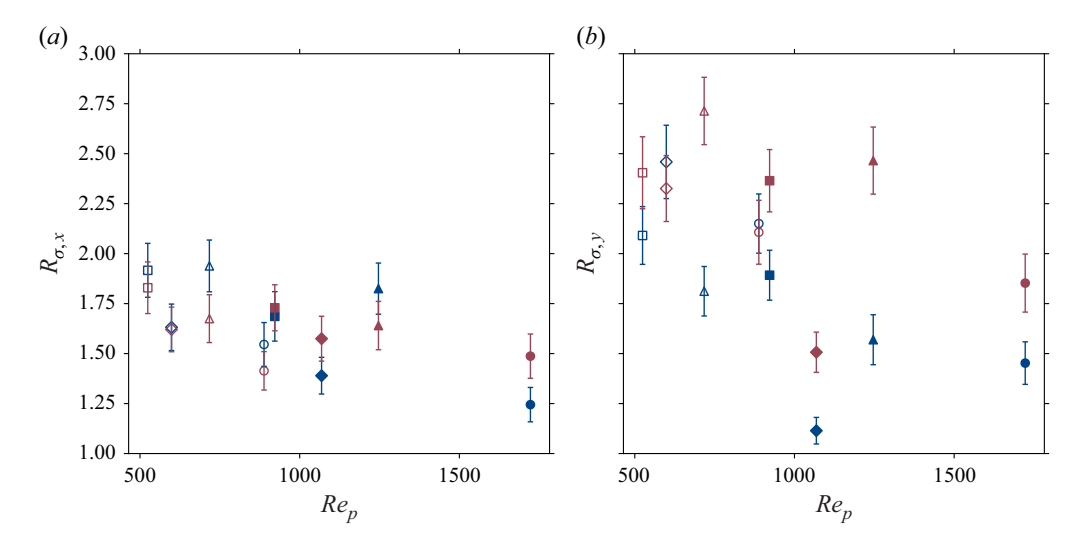


Figure 6. Particle dispersion ratios of high-to-low turbulence in (a) streamwise and (b) spanwise directions. Blue () and red () markers correspond to $U_{\infty} = 0.25 \text{ m s}^{-1}$ and 0.38 m s^{-1} , respectively. Circle , spheres; triangle , circular cylinders; diamond , square cylinders; square , flat cuboids. Solid markers, 9 mm particles; hollow markers, 6 mm particles. Error bars correspond to standard deviations computed using bootstrapping.

retarding effect of turbulence diminishes as ρ_p/ρ_f increases, the magnitude of which is comparatively very high in the present study. Applying the method of least squares reveals that $W_e \approx c_1 |W_s|$, where $c_1 = 0.941 \pm 0.005$. This linear relationship between the mean settling velocity estimated by \overline{x}_p and the quiescent settling velocity shows that the former works well as an analogue to the latter. Therefore, obtaining a reasonable prediction of \overline{x}_p using only $|W_s|$, U_b and h is possible.

Although W_e is useful in comparing the mean settling velocity between different turbulent flows, it is effectively an integral value that integrates the particle's motion linearly over time and space using bulk velocity and total particle mean displacement. It does not account for the instantaneous changes in the particle velocity due to the turbulent structures, the initial transient period wherein a particle accelerates from rest, or the effects of the developing turbulent boundary layer on the particle dynamics near the wall (see Tee & Longmire 2024). As such, W_e is only used to compare the mean settling behaviour between the turbulence levels, as it does not consider the instantaneous settling dynamics.

5. Particle dispersion

Even though the overall mean settling location of the finite-size particles remains constant with turbulence, their dispersion is highly dependent on it. The ratio of dispersion between high and low turbulence conditions, $R_{\sigma} = \sigma_{\rm h}/\sigma_{\rm l}$, in the streamwise and spanwise directions are plotted against the particle Reynolds number, $Re_p = |W_s|l_1/\nu$, in figures 6(a) and 6(b), respectively. This ratio, R_{σ} , is above unity for all particles, indicating that increasing turbulence intensity increases dispersion. This positive correlation also agrees well with the existing literature (Fornari *et al.* 2016; Esteban *et al.* 2020; Chan *et al.* 2021). There is a trend in which particles with higher values of Re_p experience a lower relative increase in dispersion by the added turbulence. Indeed, when l_1 is increased from 6 to 9 mm, R_{σ} is decreased for almost every particle shape. This result agrees well with the experimental findings of Wang & Stock (1993) who found that heavier particles tend to

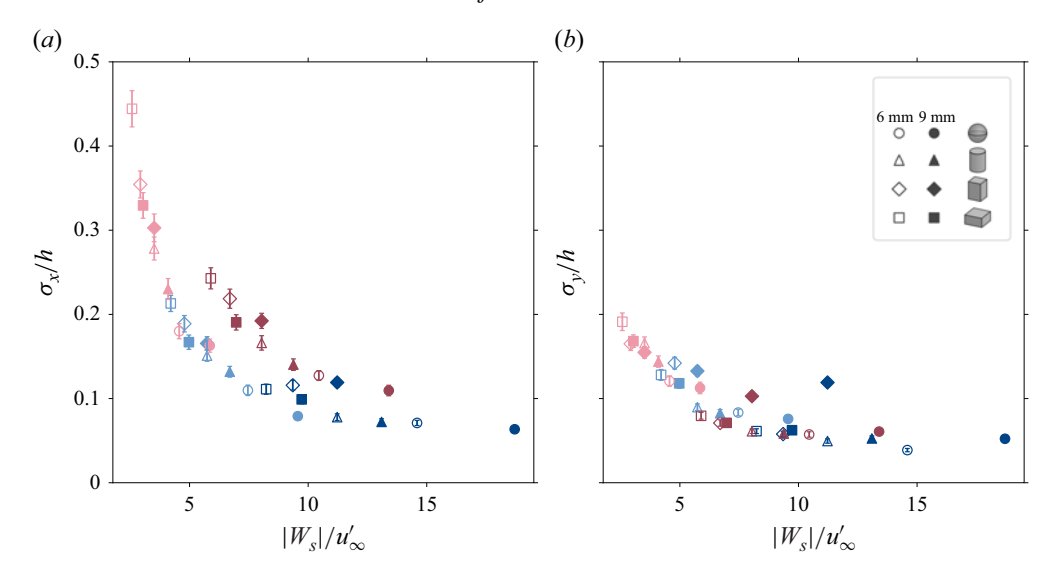


Figure 7. (a) Streamwise dispersion (σ_x) and (b) spanwise dispersion (σ_y) normalised by drop height h plotted against the ratio of settling velocity to turbulent fluctuations $(|W_s|/u_\infty')$. Dark blue (\bullet) and light blue (\bullet) markers correspond to low and high turbulence intensity at $U_\infty \approx 0.25 \text{ m s}^{-1}$, respectively, while dark red (\bullet) and pink (\bullet) markers correspond to low and high turbulence at $U_\infty \approx 0.38 \text{ m s}^{-1}$. Error bars are standard deviations of σ_x and σ_y computed using bootstrapping.

disperse less in settling-dominated flow regimes, Shin & Koch (2005) who found that dispersion decreased with particle size, and Chan $et\ al.$ (2021) who similarly found that dispersion decreased with Ar. Clark $et\ al.$ (2023) also found that dispersion was less sensitive to gravity waves with increasing particle size.

As can be seen in figure 6(a), the dispersion ratio in the streamwise direction, $R_{\sigma,x}$, is larger for certain particle geometries. Generally, flat cuboids (\blacksquare) and circular cylinders (\blacktriangle) tend to be more affected by changes in turbulent conditions compared with square cylinders (\spadesuit) and spheres (\spadesuit). In this flow regime, inertial and size effects ensure that particle-flow interactions are characterised by wakes, and their dynamics are therefore complex. Both square and circular cylinders have similar values of l_1 and l_2 . Despite this, they exhibit very different behaviours when placed in turbulent flow, suggesting particle shape has a similar, if not greater, influence on dispersion than size.

The streamwise and spanwise particle dispersion (σ_x, σ_y) normalised by the drop height is plotted against the ratio $|W_s|/u_\infty'$ in figures 7(a) and 7(b), respectively. In general, dispersion in both directions decreases exponentially with an increase in $|W_s|/u_\infty'$. This suggests an inverse relationship between a particle's settling velocity and dispersion. When comparing between σ_x and σ_y , it is clear that $\sigma_x/\sigma_y \ge 1$ for all particles. This is because anisotropy is present in the free stream with $(u'/v')_\infty > 1$ (assuming $v_\infty' \sim w_\infty'$). In HIT, turbulent fluctuations are statistically independent of direction. This is not the case for turbulent advecting flows. Hence, particles are not expected to disperse equally in the x-and y-directions. This is to say that, even though $R_{\sigma,y} > R_{\sigma,x}$ in many cases, as shown in figure 6, both the absolute dispersion and the absolute increase in dispersion with turbulence are larger in the streamwise direction than the spanwise direction.

The decreasing relationship between σ_x and $|W_s|$, as seen in figure 7, does not hold true in all flow cases for particles of different shapes. To highlight this effect, figure 7 is replotted as separate figures in figure 8 for different flow cases. Focusing on three out

P.R. Benonisen, R.J. Hearst and Y.H. Tee

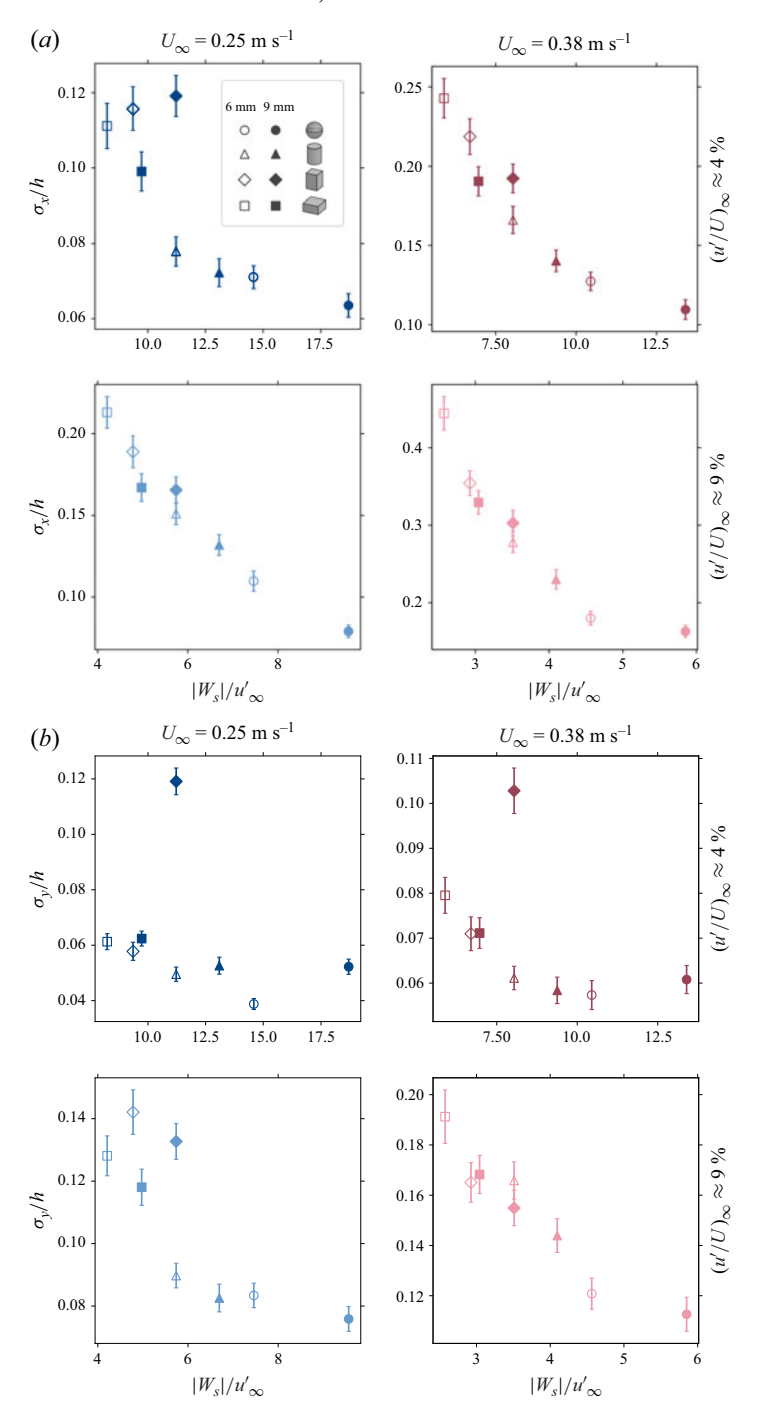


Figure 8. (a) Streamwise dispersion (σ_x) and (b) spanwise dispersion (σ_y) normalised by drop height h plotted against the ratio of settling velocity to turbulent fluctuations $(|W_s|/u_\infty')$. Error bars are standard deviations of σ_x and σ_y computed using bootstrapping.

of four particle shapes in figure 7(a) (excluding square cylinders \spadesuit), similar to what was observed earlier, there is a clear decreasing trend of σ_x with increasing $|W_s|$. Specifically, in all flow conditions, flat cuboids (which have the lowest value of $|W_s|$) are more dispersed than circular cylinders, which in turn are more dispersed than spheres (which have the highest value of $|W_s|$). The trend also holds for σ_y in figure 7(b) with the exception of 9 mm spheres at $U_{\infty} = 0.25 \text{ m s}^{-1}$. In this context, it can be hypothesised that particles with lower settling velocities remain suspended longer in the flow, giving them more opportunities to be randomly dispersed by turbulence.

However, in figure 8, it is clear that the square cylinders (♦) deviate from this strictly decreasing trend at lower values of U_{∞} and $(u'/U)_{\infty}$. At $(u'/U)_{\infty} = 4\%$, the square cylinders disperse more during their descent than the flat cuboids, despite settling farther upstream, supporting the notion that particle dispersion is not simply a product of the time spent suspended in the turbulent flow. Further confirmation of this can be found from the Gaussian-like distributions of figure 4. If particles that spent more time in the flow were more dispersed as a rule, then one could expect the probability distributions to feature long tails downstream of the peak, which is not observed here. Therefore, it is important to incorporate particle geometry in dispersion models at certain values of U_{∞} and $(u'/U)_{\infty}$, or one could risk underestimating the spread of certain particles. As the free stream velocity and turbulence intensity increase, a more robust trend appears between σ_x/h and $|W_s|$. This is due to $R_{\sigma,x}$ (see figure 6) being lower for square cylinders than for the other anisotropic particles, ensuring that the dispersion of flat cuboids overtakes that of square cylinders as $(u'/U)_{\infty}$ is elevated. This 'stabilising' effect obtained by increasing free stream turbulence happens sooner for smaller particles. By increasing either U_{∞} to $0.38 \,\mathrm{m \ s^{-1}}$ or $(u'/U)_{\infty}$ to 9 %, the dispersion of 6 mm flat cuboids has already increased beyond that of square cylinders. The 9 mm particles take longer to reach this regime. It is only when both U_{∞} and $(u'/U)_{\infty}$ are increased that the square cylinders adhere to the same trend as the other particles. These results show that the settling velocity of a particle becomes a more accurate predictor of dispersion as turbulence increases. Thus, at high values of Re_D and $(u'/U)_{\infty}$, it is enough to know a particle's characteristic size and settling velocity to estimate its dispersion. This is not to say that the effects of particle geometry are not important, however, they do become more predictable.

To provide a more quantitative assessment of the relationship between the dispersion of particles, their characteristics and free stream turbulence conditions, the scaling parameter σ_x/h was fit against dimensional parameters via regression analysis. Clark *et al.* (2023) used best subsets linear regression to identify the relative importance of different particle parameters. In the present discussion, a nonlinear approach similar to Berk *et al.* (2018) is employed to generate an empirical model based on both particle and flow parameters. The parameters used in the fit are the particle size, l_1 , the particle settling velocity, $|W_s|$, the r.m.s. of the turbulent fluctuations, u'_{∞} , the integral length scale estimate, L_{11} , kinematic viscosity, ν , and gravitational acceleration, g. The flow parameters, u'_{∞} and L_{11} , are both taken in the quasihomogeneous region. As ν and g remained relatively constant, they could not be reliably fit using nonlinear regression. Instead, they are included to balance the fit dimensionally. These parameters were chosen based on observations concerning how particle parameters and turbulence affect dispersion. The resulting nonlinear fit has the form

$$\frac{\sigma_x}{h} = A \left(l_1^{\alpha_1} |W_s|^{\alpha_2} (u_\infty')^{\alpha_3} L_{11}^{\alpha_4} v^{\alpha_5} g^{\alpha_6} \right) \pm e, \tag{5.1}$$

where $\alpha_1, \ldots, \alpha_6$ are fitted exponents, A is a constant and e is the r.m.s. of the residuals. The results of the nonlinear fit are listed in table 3. Note that l_2 is not among the variables

\boldsymbol{A}	α_1	α_2	α_3	$lpha_4$	α_5	α_6	e
50.5	0.2	-1.5	1.5	-0.5	0.2	-0.1	0.018

Table 3. Fitted coefficients for (5.1) using nonlinear regression.

included in 5.1, and as such, the aspect ratio does not appear in any of the following equations. Analysis of the data using different combinations of particle parameters $(l_1, l_2 \text{ and } | W_s|)$ to create a nonlinear fit yielded the best results when l_2 was excluded, suggesting that AR makes a less accurate predictor of dispersion than l_1 or $|W_s|$. This may be because the aspect ratio only varied in the range $0.5 \lesssim AR \lesssim 1.5$ in the present study, which may have been insufficient to identify aspect ratio effects. The particles were specifically designed to all have approximately the same aspect ratio.

With six variables and two dimensions (length and time), four non-dimensional groups can potentially be obtained according to the Buckingham Π theorem. In this discussion, two different non-dimensional groupings are presented to gain insight into particle—turbulence interaction. The first grouping uses the ratio of turbulent velocity fluctuations to the settling velocity $(u_{\infty}'/|W_s|)$ and the particle length scale to turbulent integral length scale ratio (l_1/L_{11}) ,

$$\frac{\sigma_x}{h} = A \left(\frac{u_\infty'}{|W_s|} \right)^{1.5} \left(\frac{l_1}{L_{11}} \right)^{0.5} \left(\frac{v^2}{l_1^3 g} \right)^{0.1}. \tag{5.2}$$

The third term is inversely proportional to the Archimedes number, $Ar = (\rho_p/\rho_f - 1)gl_1^3/v^2$. The Archimedes number is the square of the Galileo number, Ga, a ratio of gravitational forces to viscous forces. Substituting Ar into (5.2) yields

$$\frac{\sigma_x}{h} = B \left(\frac{u_\infty'}{|W_s|} \right)^{1.5} \left(\frac{l_1}{L_{11}} \right)^{0.5} A r^{-0.1}, \tag{5.3}$$

where $B = A(\rho_p/\rho_f - 1)^{0.1}$. The empirical expression in (5.3) is plotted against experimentally obtained values in figure 9. Most cases lie within the 95% confidence interval with decreasing relative errors as U_{∞} and $(u'/U)_{\infty}$ increase. As such, (5.3) yields better predictions at higher turbulence levels and advection velocities. The differences in anisotropy between flow cases suggest that the addition of w' to (5.3) may have some higher-order effects on the dispersion. However, while substituting u'_{∞} with an approximation of turbulent kinetic energy, $k = 1/2(u'_{\infty}^2 + 2w'_{\infty}^2)$, yields increased scatter in the data, it does not significantly alter the overall trend.

There is some elegance to the formulation of (5.3) in that it encompasses many of the physical mechanisms that one would expect from such a model. The first term $(u'_{\infty}/|W_s|)$ compares the velocity scales of the turbulence and the mean particle settling. The latter also implicitly contains information on the particle itself, as the mean settling velocity is a function of the geometry and settling dynamics. The second term (l_1/L_{11}) compares the relative length scales of the particle and the turbulence. Finally, the Archimedes number compares the relative importance of gravitational and viscous forces, which also encompasses the relative density difference between the particle and the fluid.

The scaling with $u'_{\infty}/|W_s|$ of (5.3) is in agreement with the previous discussion concerning figure 8. The sphere, which settles the fastest, has the smallest dispersion, while the flat cuboid, which settles the slowest, has the largest dispersion. In many previous

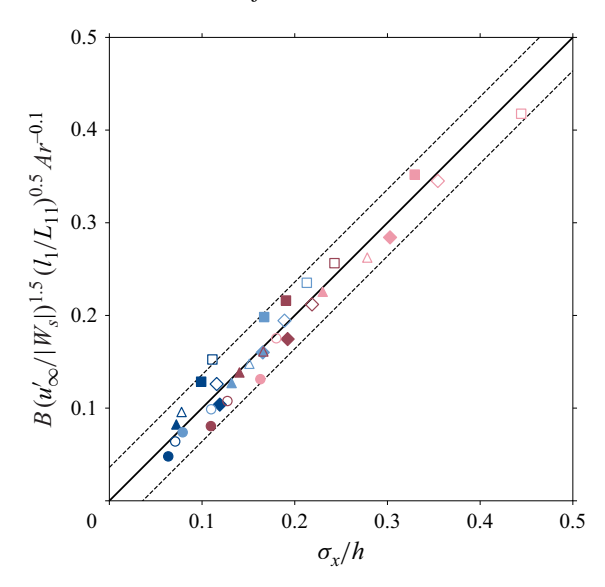


Figure 9. Equation (5.3) (solid line) plotted against experimentally determined values of σ_x/h . Dashed lines are 95 % confidence intervals. Dark blue (•) and light blue (•) markers correspond to low and high turbulence intensity at $U_\infty \approx 0.25 \text{ m s}^{-1}$, respectively, while dark red (•) and pink (•) markers correspond to low and high turbulence at $U_\infty \approx 0.38 \text{ m s}^{-1}$. Circle •, spheres; triangle \blacktriangle , circular cylinders; diamond •, square cylinders; square \blacksquare , flat cuboids. Solid markers, 9 mm particles; hollow markers, 6 mm particles.

studies concerning particle settling in turbulence, the ratio $u_{\infty}'/|W_{\delta}|$ has proven important to settling behaviour (Dávila & Hunt 2001; Good et al. 2014; Fornari et al. 2016), providing support to the validity of (5.3) even though it has not, to our knowledge, been directly tied to finite-size particle dispersion in this way. The proportionality with the square root of l_1/L_{11} might initially suggest that increasing particle size leads to an increase in dispersion, which disagrees with the present experimental results. This is due to the interdependency between the non-dimensional groups in (5.3). Specifically, changing l_1 causes a change in $|W_s|$ that is difficult to determine exactly a priori. Nevertheless, within the present experimental parameters, $|W_s|$ scales with l_1 such that increasing the particle size attenuates dispersion. Finally, the inverse proportionality with Ar entails that if one could keep the other ratios constant, a higher-volume particle would experience reduced dispersion. This agrees with Shin & Koch (2005) and Chan et al. (2021), who found an inverse relationship between dispersion and particle size. As discussed in § 1, Clark et al. (2023) also found that Ar is an important parameter when determining the effect of gravity waves on dispersion. Lastly, it should be noted that in the present study the particles' aspect ratios did not vary significantly from unity, i.e. $0.5 \le AR \le 1.5$. Studies specifically designed to investigate AR have found it to be an important parameter that influences dispersion (Njobuenwu & Fairweather 2015; DiBenedetto, Ouellette & Koseff 2018; Clark et al. 2023) and particle dynamics (Shapiro & Goldenberg 1993; Shin & Koch 2005; Tinklenberg 2024). Here, we do not conclude that AR is not an important parameter, but rather note that it was not specifically tested. Particles with AR values far outside the range of the present study may settle differently, and the application of (5.3) in such cases should be done with care.

In HIT, the dissipation rate of turbulent kinetic energy, ϵ , is related to the turbulent velocity fluctuations and the integral length scales by $\epsilon \sim (u_{\infty}')^3/L_{11}$ and is balanced by the rate of turbulent kinetic energy production (Pope 2000). Equation (5.3) can be

rearranged to be expressed in terms of ϵ to obtain

$$\frac{\sigma_x}{h} = C \left(\frac{\epsilon l_1}{|W_x|^3} \right)^{0.5} Ar^{-0.1},\tag{5.4}$$

where the constant C is introduced due to the substitution of ϵ . A common way of modelling the dispersion of suspended particles in turbulence is to equate it to a diffusive process (Brandt & Coletti 2022). Under this assumption, dispersion is proportional to the eddy diffusivity, $K \sim u_{\infty}' L_{11}$ (Tennekes & Lumley 1972). While diffusion may play a key role in other particle transport scenarios, for the inertial, finite-size particles investigated in this study, (5.4) suggests that the dispersion is not simply a diffusive process as σ_x increases with ϵ rather than K. This emphasises the importance of taking into account particle size and inertia when developing numerical models.

6. Conclusions

In this experimental study, the advection and dispersion of negatively buoyant finite-size spherical and non-spherical particles in turbulent open channel flow have been investigated. Eight different particles of four geometries (spheres, circular cylinders, square cylinders, flat cuboids) and two sizes (6 and 9 mm) are considered. The results based on their settling locations have yielded insight into their behaviour when travelling in different turbulent conditions. It was found that the average distance particles are advected before being deposited, \bar{x}_p , is primarily a function of the bulk velocity and the particle settling velocity in quiescent flow. Altering the turbulence level had little to no effect on \bar{x}_p . From this, it can also be inferred that, even though individual particle trajectories are distinct, the average vertical velocity is independent of the turbulent fluctuations in the present particle—turbulence regime.

In contrast, the dispersion of particles increases with turbulence in all cases. The level of enhancement was found to be highly dependent on particle geometry and size. Generally, increasing particle size resulted in reduced sensitivity to changing turbulence levels, with the dispersion ratio, R_{σ} , being smaller for higher values of l_1 . Framing this relative to the Stokes number, St, increasing the l_1 results in higher St, and thus the diminishing effect of turbulence falls in line with expectations. Circular cylinders and flat cuboids are more sensitive to turbulence changes than square cylinders and spheres. This result was observed despite circular and square cylinders having similar aspect ratios, highlighting the importance of particle geometry in determining dispersion.

For the majority of the particles considered, the streamwise and spanwise dispersion (σ_x, σ_y) decrease with the mean settling velocity $(|W_s|)$. From this, it can be hypothesised that dispersion is partially a function of time spent suspended in the turbulent flow. Although the settling velocity is a good predictor of σ_x at high flow speeds and turbulence levels, not all particles adhere to this relationship. The square cylinders are much more dispersed than the flat cuboids at low values of U_∞ and $(u'/U)_\infty$, despite settling faster. This phenomenon is amplified by particle size, with 6 mm particles more readily conforming to a monotonic decrease in σ_x with $|W_s|$ at higher values of U_∞ and $(u'/U)_\infty$ than 9 mm particles.

To quantify the interplay between turbulent conditions and particle dispersion, a nonlinear fit relating σ_x to turbulent fluctuations, integral length scale, particle settling velocity and particle size is proposed. This fit confirms the importance of $u_{\infty}'/|W_s|$ as in earlier studies of small inertial particles, such that particle dispersion increases with turbulent velocity fluctuations while decreasing with the settling velocity. Increasing the particle size leads to higher settling velocities, which in turn causes a decrease in

dispersion. Another possible interpretation of the empirical relation is that σ_x scales with the turbulent kinetic energy dissipation rate, $\epsilon \sim (u_\infty')^3/L_{11}$. This stands in contrast to a purely diffusive process wherein particle dispersion is proportional to the eddy diffusivity, $K \sim u_\infty' L_{11}$.

The geometries and sizes of plastic waste in the ocean are diverse and varied. In modelling the dispersion of negatively buoyant finite-size particles in turbulent flows, the present results show that size and geometry effects must be considered. Even though shape effects are 'stabilised' at higher turbulence levels and Reynolds numbers, assuming a monotonic reduction in dispersion with settling velocity can lead to underestimating the spread of particles in certain turbulent conditions. Nonetheless, there appears to be some universality governing the underlying physical mechanisms.

Acknowledgements. The authors thank Dr K. Muller (ETH Zürich) for the assistance in adapting his particle tracking software to the present study, and Dr L.K. Clark Sunberg (CU Boulder) for her input on developing the experimental set-up.

Data availability. The data from this study are available at https://doi.org/10.18710/2RFUMU.

Funding. Y.H.T. and R.J.H. are funded by the European Union (MSCA-PF 101107440, InMyWaves; ERC StG 101041000, GLITR). Views and opinions expressed are, however, those of the authors only and do not necessarily reflect those of the European Union, the Research Executive Agency or the European Research Council. Neither the European Union nor the granting authority can be held responsible for them.

Declaration of interests. The authors report no conflict of interest.

REFERENCES

- AUGUSTE, F., MAGNAUDET, J. & FABRE, D. 2013 Falling styles of disks. J. Fluid Mech. 719, 388–405.
- BAKER, L.J. & COLETTI, F. 2021 Particle-fluid-wall interaction of inertial spherical particles in a turbulent boundary layer. *J. Fluid Mech.* **908**, A39.
- BAKER, L.J. & COLETTI, F. 2022 Experimental investigation of inertial fibres and disks in a turbulent boundary layer. *J. Fluid Mech.* **943**, A27.
- BALACHANDAR, S. & EATON, J.K. 2010 Turbulent dispersed multiphase flow. Annu. Rev. Fluid Mech. 42 (1), 111-133.
- BERK, T., HUTCHINS, N., MARUSIC, I. & GANAPATHISUBRAMANI, B. 2018 Trajectory of a synthetic jet issuing into high-Reynolds-number turbulent boundary layers. *J. Fluid Mech.* **856**, 531–551.
- Bragg, A.D., RICHTER, D.H. & WANG, G. 2021 Mechanisms governing the settling velocities and spatial distributions of inertial particles in wall-bounded turbulence. *Phys. Rev. Fluids.* **6**, 065302.
- BRANDT, L. & COLETTI, F. 2022 Particle-laden turbulence: progress and perspectives. Annu. Rev. Fluid Mech. 54 (1), 159–189.
- BUCHNER, A.-J., MULLER, K., MEHMOOD, J. & TAM, D. 2021 Hopping trajectories due to long-range interactions determine surface accumulation of microalgae. *Proceedings of the National Academy of Sciences.* 118 (20), e2102095118.
- CASTRO, I.P. 2007 Rough-wall boundary layers: mean flow universality. J. Fluid Mech. 585, 469–485.
- CHAN, T.T.K., ESTEBAN, L.B., HUISMAN, S.G., SHRIMPTON, J.S. & GANAPATHISUBRAMANI, B. 2021 Settling behaviour of thin curved particles in quiescent fluid and turbulence. *J. Fluid Mech.* **922**, A30.
- CLARK, L.K., DIBENEDETTO, M.H., OUELLETTE, N.T. & KOSEFF, J.R. 2023 Dispersion of finite-size, non-spherical particles by waves and currents. J. Fluid Mech. 954, A3.
- CLIFT, R., GRACE, J.R. & WEBER, M.E. 1992 Bubbles, drops, and particles, 3rd edn.
- COMTE-BELLOT, G. & CORRSIN, S. 1966 The use of a contraction to improve the isotropy of grid-generated turbulence. *J. Fluid Mech.* **25** (4), 657–682.
- CRESSEY, D. 2016 Bottles, bags, ropes and toothbrushes: the struggle to track ocean plastics. *Nature* **536** (7616), 263–265.
- DIBENEDETTO, M.H., OUELLETTE, N.T. & KOSEFF, J.R. 2018 Transport of anisotropic particles under waves. J. Fluid Mech. 837, 320–340.
- DÁVILA, J. & HUNT, J.C.R. 2001 Settling of small particles near vortices and in turbulence. J. Fluid Mech. 440, 117–145.

P.R. Benonisen, R.J. Hearst and Y.H. Tee

- ESTEBAN, L.B., DOGAN, E., RODRÍGUEZ-LÓPEZ, E. & GANAPATHISUBRAMANI, B. 2017 Skin-friction measurements in a turbulent boundary layer under the influence of free-stream turbulence. *Exp. Fluids.* **58** (9), 115.
- ESTEBAN, L.B., SHRIMPTON, J.S. & GANAPATHISUBRAMANI, B. 2020 Disks settling in turbulence. *J. Fluid Mech.* 883, A58.
- FERRAN, A., MACHICOANE, N., ALISEDA, A. & OBLIGADO, M. 2023 An experimental study on the settling velocity of inertial particles in different homogeneous isotropic turbulent flows. *J. Fluid Mech.* **970**, A23.
- FORNARI, W., PICANO, F., SARDINA, G. & BRANDT, L. 2016 Reduced particle settling speed in turbulence. J. Fluid Mech. 808, 153–167.
- GALGANI, F., HANKE, G. & MAES, T. 2015 Global distribution, composition and abundance of marine litter. In *Marine Anthropogenic Litter*, (ed. M. Bergmann, L. Gutow & M. Klages), pp. 29–56.
- GIURGIU, V., CARIDI, G.C.A., DE PAOLI, M. & SOLDATI, A. 2024 Full rotational dynamics of plastic microfibers in turbulence. *Phys. Rev. Lett.* **133** (5), 054101.
- GOOD, G., IRELAND, P., BEWLEY, G., BODENSCHATZ, E., COLLINS, L. & WARHAFT, Z. 2014 Settling regimes of inertial particles in isotropic turbulence. *J. Fluid Mech.* 759, R3.
- GORAL, K.D., GULER, H.G., LARSEN, B.E., CARSTENSEN, S., CHRISTENSEN, E.D., KERPEN, N.B., SCHLURMANN, T. & FUHRMAN, D.R. 2023 Settling velocity of microplastic particles having regular and irregular shapes. *Environ. Res.* 228, 115783.
- GUSTAVSSON, K., EINARSSON, J. & MHELIG, B. 2014 Tumbling of small axisymmetric particles in random and turbulent flows. *Phys. Rev. Lett.* **112**, 014501.
- HEARST, R.J. & LAVOIE, P. 2015 The effect of active grid initial conditions on high Reynolds number turbulence. *Exp. Fluids.* **56** (10), 185.
- VAN HOUT, R. 2013 Spatially and temporally resolved measurements of bead resuspension and saltation in a turbulent water channel flow. *J. Fluid Mech.* **715**, 389–423.
- VAN HOUT, R., HERSHKOVITZ, A., ELSINGA, G.E. & WESTERWEEL, J. 2022 Combined three-dimensional flow field measurements and motion tracking of freely moving spheres in a turbulent boundary layer. *J. Fluid Mech.* **944**, A12.
- JEFFERY, G.B. 1922 The motion of ellipsoidal particles immersed in a viscous fluid. *Proceedings of the Royal Society of London. Series A, Containing Papers of a Mathematical and Physical Character.* **102** (715), 161–179.
- JIMÉNEZ, J. 1997 Oceanic turbulence at millimeter scales. Sci. Mar. 61, 47-56.
- JOOSS, Y., LI, L., BRACCHI, T. & HEARST, R.J. 2021 Spatial development of a turbulent boundary layer subjected to freestream turbulence. J. Fluid Mech. 911, A4.
- KAISER, D., KOWALSKI, N. & WANIEK, J.J. 2017 Effects of biofouling on the sinking behavior of microplastics. *Environ. Res. Lett.* 12 (12), 124003.
- LARSSEN, J.V. & DEVENPORT, W.J. 2011 On the generation of large-scale homogeneous turbulence. *Exp. Fluids*. **50** (5), 1207–1223.
- MAKITA, H. 1991 Realization of a large-scale turbulence field in a small wind tunnel. *Fluid Dyn. Res.* **8** (1–4), 53.
- MAXEY, M.R. 1987 The gravitational settling of aerosol particles in homogeneous turbulence and random flow fields. *J. Fluid Mech.* **174**, 441–465.
- MULLER, K., HEMELRIJK, C.K., WESTERWEEL, J. & TAM, D.S.W. 2020 Calibration of multiple cameras for large-scale experiments using a freely moving calibration target. *Exp. Fluids.* **61** (1), 7.
- NIELSEN, P. 1993 Turbulence effects on the settling of suspended particles. *J. Sediment. Res.* **63** (5), 835–838. NJOBUENWU, D. & FAIRWEATHER, M. 2015 Dynamics of single, non-spherical ellipsoidal particles in a turbulent channel flow. *Chem. Eng. Sci.* **123**, 265–282.
- Petersen, A.J., Baker, L. & Coletti, F. 2019 Experimental study of inertial particles clustering and settling in homogeneous turbulence. *J. Fluid Mech.* 864, 925–970.
- POPE, S.B. 2000 Turbulent flows.
- PRATA, J.C., DA COSTA, J.P., LOPES, I., DUARTE, A.C. & ROCHA-SANTOS, T. 2020 Environmental exposure to microplastics: an overview on possible human health effects. *Sci. Total Environ.* **702**, 134455.
- RODRÍGUEZ-LÓPEZ, E., BRUCE, P.J.K. & BUXTON, O.R.H. 2015 A robust post-processing method to determine skin friction in turbulent boundary layers from the velocity profile. *Exp. Fluids.* **56** (4), 68.
- SCHNEIDERS, J.F.G. & SCIACCHITANO, A. 2017 Track benchmarking method for uncertainty quantification of particle tracking velocimetry interpolations. *Meas. Sci. Technol.* 28 (6), 065302.
- SHAIK, S. & VAN HOUT, R. 2023 Kinematics of rigid fibers in a turbulent channel flow. *Int. J. Multiphase Flow.* **158**, 104262.
- SHAPIRO, M. & GOLDENBERG, M. 1993 Deposition of glass fiber particles from turbulent air flow in a pipe. J. Aerosol Sci. 24 (1), 65–87.

- SHIN, M. & KOCH, D.L. 2005 Rotational and translational dispersion of fibres in isotropic turbulent flows. J. Fluid Mech. 540, 143–173.
- SQUIRES, K.D. & EATON, J.K. 1991 Preferential concentration of particles by turbulence. *Phys. Fluids A*. 3 (5), 1169–1178.
- SUMER, B.M. 1974 Mean velocity and longitudinal dispersion of heavy particles in turbulent open-channel flow. *J. Fluid Mech.* **65** (1), 11–28.
- SUNBERG, L.K.C., DIBENEDETTO, M.H., OUELLETTE, N.T. & KOSEFF, J.R. 2024 Parametric study of the dispersion of inertial ellipsoidal particles in a wave-current flow. *Phys. Rev. Fluids.* **9** (3), 034302.
- SUTHERLAND, B.R., DIBENEDETTO, M., KAMINSKI, A. & VAN DEN BREMER, T. 2023 Fluid dynamics challenges in predicting plastic pollution transport in the ocean: a perspective. *Phys. Rev. Fluids.* 8 (7), 070701.
- TEE, Y.H., BARROS, D.C. & LONGMIRE, E.K. 2020 Motion of finite-size spheres released in a turbulent boundary layer. *Int. J. Multiphase Flow.* **133**, 103462.
- TEE, Y.H., DAWSON, J.R. & HEARST, R.J. 2025 Volumetric study of particle-wake interactions based on free falling finite particles. *Exp. Fluids*. **66** (7), 1–13.
- TEE, Y.H. & LONGMIRE, E.K. 2024 Effect of fluid motions on finite spheres released in turbulent boundary layers. *J. Fluid Mech.* **985**, A28.
- TENNEKES, H. & LUMLEY, J.L. 1972 A first course in turbulence.
- TINKLENBERG, A. 2024 Experimental investigation of disks settling in quiescent and turbulent air. PhD thesis, University of Minnesota.
- TINKLENBERG, A., GUALA, M. & COLETTI, F. 2024 Turbulence effect on disk settling dynamics. *J. Fluid Mech.* **992**, A4.
- TOM, J. & BRAGG, A.D. 2019 Multiscale preferential sweeping of particles settling in turbulence. J. Fluid Mech. 871, 244–270.
- VOTH, G.A. & SOLDATI, A. 2017 Anisotropic particles in turbulence. Annu. Rev. Fluid Mech. 49 (1), 249–276.
 WANG, L.-P. & STOCK, D.E. 1993 Dispersion of heavy particles by turbulent motion. J. Atmos. Sci. 50 (13), 1897–1913.
- WESTERWEEL, J., GEELHOED, P. & LINDKEN, R. 2004 Single-pixel resolution ensemble correlation for micro-PIV applications. *Exp. Fluids*. **37** (3), 375–384.
- WIENEKE, B. 2015 PIV uncertainty quantification from correlation statistics. *Meas. Sci. Technol.* **26** (7), 074002.